

Journal of Geophysical Research: Space Physics

RESEARCH ARTICLE

10.1002/2016JA023512

Special Section:

Major Results From the MAVEN Mission to Mars

Key Points:

- A new algorithm specifies variations of solar EUV irradiance at Mars with typical relative uncertainties near 5%
- Daily average and flare irradiances are derived from SDO EVE measurements from 6 to 106 nm
- Examples of EUV variability for the MAVEN primary mission are presented

Supporting Information:

- Supporting Information S1
- Data Set S1
- Data Set S2

Correspondence to:

E. M. B. Thiemann,
thiemann@lasp.colorado.edu

Citation:

Thiemann, E. M. B., P. C. Chamberlin, F. G. Eparvier, B. Templeman, T. N. Woods, S. W. Bouger, B. M. Jakosky (2017), The MAVEN EUVM model of solar spectral irradiance variability at Mars: Algorithms and results, *J. Geophys. Res. Space Physics*, 122, doi:10.1002/2016JA023512.

Received 24 SEP 2016

Accepted 28 FEB 2017

Accepted article online 9 MAR 2017

The MAVEN EUVM model of solar spectral irradiance variability at Mars: Algorithms and results

Edward M. B. Thiemann¹ , Phillip C. Chamberlin² , Francis G. Eparvier¹ , Brian Templeman¹, Thomas N. Woods¹, Stephen W. Bouger³ , and Bruce M. Jakosky¹ 

¹Laboratory for Atmospheric and Space Physics, University of Colorado Boulder, Boulder, Colorado, USA, ²Solar Physics Laboratory, NASA Goddard Spaceflight Center, Greenbelt, Maryland, USA, ³Department of Climate and Space Sciences and Engineering, University of Michigan, Ann Arbor, Michigan, USA

Abstract Solar extreme ultraviolet (EUV) radiation is a primary energy input to the Mars atmosphere, causing ionization and driving photochemical processes above approximately 100 km. Because solar EUV radiation varies with wavelength and time, measurements must be spectrally resolved to accurately quantify its impact on the Mars atmosphere. The Mars Atmosphere and Volatile Evolution (MAVEN) EUV Monitor (EUVM) measures solar EUV irradiance incident on the Mars atmosphere in three bands. These three bands drive a spectral irradiance variability model called the Flare Irradiance Spectral Model (FISM)-Mars (FISM-M) which is an iteration of the FISM model by Chamberlin et al. (2007, 2008) for spectral irradiance at Earth. In this paper, we report the algorithms used to derive FISM-M and its associated uncertainties, focusing on differences from the original FISM. FISM-M spectrally resolves the solar EUV irradiance at Mars from 0.5 to 189.5 nm at 1 min cadence, and 0.1 nm resolution in the 6–106 nm range or 1 nm resolution otherwise. FISM-M is suitable for both daily average and flaring spectral irradiance estimates and is based on the linear association of the broadband EUVM measurements with spectral irradiance measurements, including recent high time cadence 0.1 nm resolution measurements from the EUV Variability Experiment (EVE) on the Space Dynamics Observatory (SDO) between 6 and 106 nm. In addition, we present examples of model outputs for EUV irradiance variability due to solar flares, solar rotations, Mars orbit eccentricity, and the solar cycle, between October 2015 and November 2016.

1. Introduction

Mars is believed to have once had substantial amounts of flowing water which would have required a thicker and warmer atmosphere than is currently present [e.g., Jakosky and Phillips, 2001; Carr and Head, 2003]. All planets lose some portion of their atmosphere to space, and those that lack a global magnetic field, like Mars, are particularly sensitive to erosion by the solar wind, which would otherwise be deflected around a planet with a strong global magnetic field [Chassefière and Leblanc, 2004]. As such, Mars could have lost a significant fraction of its atmosphere and water to space over time. The National Aeronautics and Space Administration (NASA) sent the Mars Atmosphere and Volatile Evolution (MAVEN) spacecraft to Mars to characterize the mechanisms and magnitude of atmospheric escape in the current epoch in order to better understand how the Martian atmosphere has evolved over time [Jakosky et al., 2015].

MAVEN was launched on 18 November 2013 and began its primary science mission at Mars on 17 November 2014. MAVEN is instrumented to characterize the Mars upper atmosphere and plasma environment as well as the solar drivers that influence it, providing a single platform to measure both escaping atoms and ions and the drivers that lead to escape. The MAVEN orbit is highly elliptical with apoapsis near 6000 km and periapsis near 150 km, and it precesses so that in situ periapsis measurements sample the thermosphere and ionosphere over a range of local times and latitudes, or conversely, in situ apoapsis measurements sample a range of regions of the near-space environment, including the solar wind, magnetosheath, and magnetotail.

Along with the solar wind, solar extreme ultraviolet (EUV, 6–120 nm) radiation is a primary energy input to the Mars upper atmosphere, heating the thermosphere, creating the ionosphere, and constraining processes that lead to atmospheric escape to space [Bouger et al., 2015a]. Photons with wavelengths below approximately 100 nm are strongly absorbed by neutral CO₂ and O, which together constitute the major species of the Mars

upper atmosphere. The abundance of these species results in total absorption of the solar EUV spectrum above approximately 100 km with peak energy deposition occurring near 150 km [Haider and Mahajan, 2014].

MAVEN characterizes the solar EUV radiation input at Mars with the Extreme Ultraviolet Monitor (EUVM), a sensor on the Langmuir Probes and Waves (LPW) instrument [Eparvier et al., 2015]. EUVM has three calibrated photometers that measure solar irradiance at Mars in the 0–7 nm, 17–22 nm, and 117–125 nm (full width at half maximum (FWHM)) bands at 1 s cadence. Solar irradiance is defined as the solar radiated power per unit area incident on a surface or, in the case of spectral irradiance, power per unit area per unit wavelength with SI units of W m^{-2} or $\text{W m}^{-2} \text{nm}^{-1}$, respectively. The EUVM bands were selected to measure variability in three different regions of the solar atmosphere, and serve as proxies, or inputs, for an EUV spectral model from 0.5 to 189.5 nm with 0.1 nm resolution from 6 to 106 nm and 1 nm resolution otherwise. Here we adopt a convention similar to that of Tobiska et al. [2000] and Chamberlin et al. [2007, 2008] and define a proxy to be any solar measurement that is used in combination with regression coefficients to estimate solar spectral irradiance variability. They can be of non-EUV origin such as sunspot number or 10.7 cm solar radio flux ($F_{10.7}$), or they can be EUV measurements such as the three MAVEN EUVM bands. The three calibrated irradiances that are used as inputs to the EUVM spectral model are reported in the EUVM Level 2 data product, and the modeled spectral irradiance variability at Mars is produced by the Flare Irradiance Spectral Model (FISM)-Mars (M) and reported as part of the Level 3 data product. FISM-M is the focus of this paper and consists of daily and flare irradiance variability model components which will be presented separately.

FISM-M is the MAVEN EUVM spectral model and is an iteration of FISM developed by Chamberlin et al. [2007, 2008]. We will refer to the original FISM by Chamberlin et al. [2007, 2008] as FISMv1 to avoid confusion. Both FISMv1 and FISM-M model irradiance empirically with a set of linear regression coefficients that relate available proxies to spectral irradiance measurements and are found by the method of least squares. This is the same basic method used by earlier empirical EUV spectral irradiance variability models, which include Hinteregger81 [Hinteregger et al., 1981], EUVAC [Richards et al., 1994], EUV97 [Tobiska and Eparvier, 1998], Solar2000 [Tobiska et al., 2000], and HEUVAC [Richards et al., 2006].

FISM-M advances daily and flare empirical irradiance variability modeling by relating measurements of EUV irradiance variations in broad spectral bands to spectral irradiance measurements in the 6–106 nm range made by the EUV Variability Experiment (EVE) [Woods et al., 2012], which is on board the Solar Dynamics Observatory (SDO) satellite launched on 11 February 2010 and has improved spectral and temporal resolution as well as an improved responsivity calibration accuracy compared to its predecessor, Thermosphere Ionosphere Mesosphere Energetics and Dynamics (TIMED) Solar EUV Experiment (SEE) [Woods et al., 2000; Hock et al., 2012]. The 6–106 nm range is measured by EVE with the Multiple EUV Grating Spectrographs (MEGS) at 0.1 nm resolution and 10 s time cadence. MEGS observed the Sun nearly continuously in the 6–37 nm range until 27 May 2014, after which the channel suffered a failure resulting in the loss of observations in this spectral range. MEGS continues to make solar observations in the 35–106 nm range for five continuous minutes every hour which are supplemented with varying daily campaigns of extended continuous coverage lasting 3 to 24 h. In addition to including the 6–27 nm range not spectrally resolved by SEE EGS, EVE MEGS measurements in the 6–106 nm range are an improvement over those of SEE EUV Grating Spectrograph (EGS) by having 10 times better spectral resolution (0.1 nm versus 1 nm) and continuous observations at 10 s cadence compared with the 3 min observation periods every 100 min at 10 s cadence made by TIMED SEE. SDO EVE's improved observation cadence is suitable for measuring flare irradiance, which can vary by tens to hundreds of percent over a period of minutes and last tens of minutes to hours (depending on wavelength and flare magnitude). With regard to improved uncertainty, the MEGS responsivity is known to within 1–3% (1σ) uncertainty below 80 nm from preflight calibrations [Hock et al., 2012], in comparison with the 3–7% (1σ) preflight responsivity uncertainty of SEE EGS [Woods et al., 2005].

FISM-M has been widely used in the analysis of MAVEN results. For example, Rahmati et al. [2015] used EUV spectra to estimate ionization rates used in a model of O pickup ions; Chaffin et al. [2015], Chafray et al. [2015], Jain et al. [2015], Evans et al. [2015], and Deighan et al. [2015] used EUV and far ultraviolet (FUV, 120–190 nm) spectra to interpret airglow brightnesses measured by the MAVEN Imaging Ultraviolet Spectrograph (IUVS); and Sakai et al. [2016] and Peterson et al. [2016] used EUV spectra to estimate photoelectron production.

Given its improvements over FISMv1 and applicability to the analysis of MAVEN results, it is important to demonstrate the capabilities and limitations of the FISM-M data product. This paper describes the calibration and algorithms used to produce the MAVEN EUVM FISM-M data product, Version 8 Revision 1, and reports

its uncertainties and caveats. Although the model and results reported here are specific to irradiance at Mars as observed by MAVEN EUVM, they include the first reported spectral irradiance variability model based on the EVE data set and should be of interest to the broader solar irradiance and terrestrial upper atmosphere research communities.

This paper is outlined as follows: we motivate the need for spectral irradiance modeling at Mars by describing EUV variability at Mars, followed by a review of the data and sources used to develop and run FISM-M. We then provide a detailed description of FISM-M, reporting the model uncertainty and caveats. Next, FISM-M irradiance variability results from the MAVEN mission are reported, which include a model of where in the Mars atmosphere EUV energy is absorbed as a function of altitude and wavelength. We finish the paper by discussing future improvements to the FISM-M data product.

2. Estimates and Measurements of EUV Irradiance Variability at Mars

The solar EUV spectrum consists of series of emission lines and ionization continua emitted from ionized gases in the solar chromosphere, transition region, and corona. Below 10 nm, thermal bremsstrahlung continua can become significant [Phillips *et al.*, 2008]. The EUV spectrum is loosely defined as ranging from 6 to 120 nm, bracketed by the soft X-ray (SXR) and far ultraviolet (FUV) regions on the short and long edges, respectively, both of which also deposit energy into the upper atmosphere of Mars [Bougher *et al.*, 2015a]. EUV radiation varies significantly on timescales of minutes from solar flares, days from solar rotation, and years from the solar cycle [Lean, 1997]. The effect of solar activity on the EUV spectrum is not uniform, with shorter wavelengths tending to be more variable than longer wavelengths [Woods *et al.*, 2005, 2015]. This spectral dependence on variability is a result of the shorter wavelengths primarily originating in the more variable corona compared to the longer wavelengths which are primarily of chromospheric origin. Because the constituent gas ionization cross sections also vary as a function of wavelength, EUV radiation must be spectrally resolved to accurately characterize the effect it has on the Mars upper atmosphere. Mars's orbit eccentricity adds an additional 687 day (1 Mars year) variability cycle as the Mars-Sun distance changes from 1.38 to 1.67 AU. This should be contrasted with the Earth-Sun distance which varies from 0.983 to 1.017 AU over an Earth year. Both seasonal and solar cycle EUV variability is expected to be a major source of variability in the Mars upper atmosphere [Bougher *et al.*, 2015a, 2016].

EUV irradiance at Earth and Mars differs for two primary reasons. First, irradiance falls off inversely with the square of the distance from the Sun. As such, irradiance at Mars is 36–53% of that at 1 AU compared with irradiance at Earth which varies from 96.7 to 103.4% of the 1 AU value due to the planetary orbit eccentricity. Because EUVM data products are primarily intended to be used for characterizing the Mars atmosphere and the Mars orbit eccentricity is a significant contributor to irradiance variability at Mars, we report irradiance scaled to the center-to-center Mars-Sun distance unless otherwise stated in this paper. The second reason EUV irradiances at Earth and Mars differ is because EUV radiation originates from inhomogeneous features in the Sun's atmosphere such as active regions and the solar hemisphere visible from Mars may have more or less EUV source regions than the solar hemisphere visible from Earth. These solar features appear to migrate across the observed solar disk due to solar rotation, which varies with latitude and has a sidereal period of 24.4 days at the equator and 38 days at the poles. Carrington [1858] discovered that activity regions tended to be confined to certain latitudes that rotate with a sidereal period equal to 25.38 days, now known as the Carrington period, and cause irradiance variability at this timescale.

2.1. Estimating Irradiance at Mars From Earth Measurements

Irradiance can be estimated at Mars by linearly interpolating measurements from Earth made before and after the face of the Sun rotates past Mars for a particular day of interest if we assume that the source regions rotate with a constant 25.38 day period. A description of the interpolation scheme follows, using the geometrical definitions indicated in Figures 1a and 1b, where Ω_s is the solar rotation frequency taken to be $2\pi/25.38$ radian/day and Ω_E is the Earth orbital rate taken to be $2\pi/365.25$ radian/day. The interpolated irradiance at 1AU for the hemisphere of the Sun facing Mars with a Mars-Sun-Earth angle $\Theta_{ME}(t_d)$ for day t_d is given by

$$E_M(t_d, \Theta_{ME}) = (w_1 E_E(t_d - \Delta t_1) + w_2 E_E(t_d + \Delta t_2)) R_M(t_d)^{-2}, \quad (1)$$

where E_E is measured at Earth and scaled to 1 AU. Θ_{ME} is defined with counterclockwise rotation being positive, and $R_M(t_d)$ is the Mars-Sun distance in units of AU (on day t_d); values of Θ_{ME} and R_M for the first 2.25 years of the Mars mission are shown in Figures 1c and 1d.

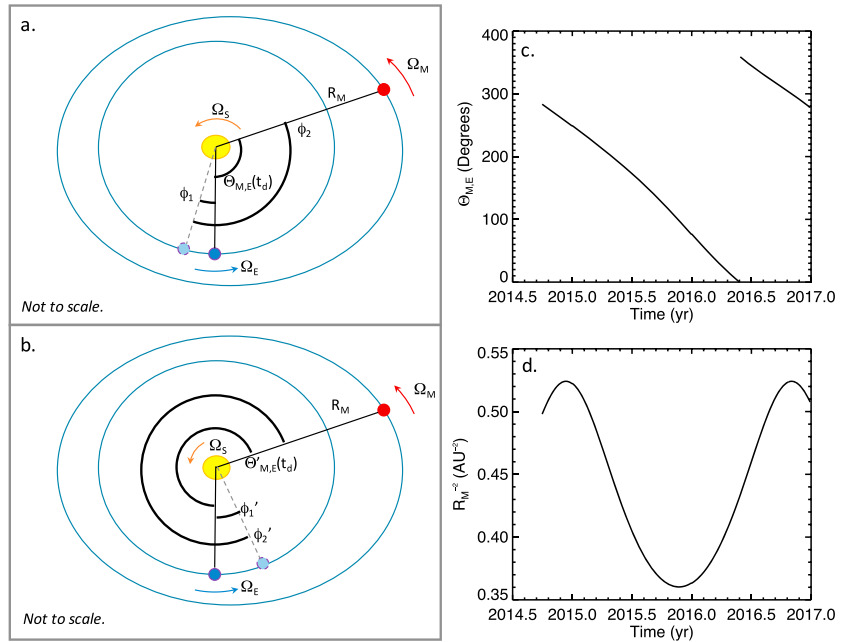


Figure 1. (a and b) Geometric definitions used to interpolate Earth-measured irradiance proxies to the Mars angular position. t_d is the day when irradiance is needed at Mars. It is found by linearly interpolating irradiance at Earth measured on days $t_d - \Delta t_1$ and $t_d + \Delta t_2$. (c) The Mars-Sun-Earth angle and (d) the Mars-Sun distance squared as a function of time during the MAVEN mission. See section 2 for details.

Beginning with the definitions in Figure 1a, we can express ϕ_1 in terms of the time difference Δt_1 .

$$\phi_1 = \Omega_E \cdot \Delta t_1. \quad (2)$$

The face of the Sun rotates at an angle ϕ_2 from Earth on day $t_d - \Delta t_1$ to Mars on day t_d at angular speed Ω_S , allowing us to write

$$\phi_2 = \Omega_S \cdot \Delta t_1. \quad (3)$$

From Figure 1a, we see that $\phi_2 = \phi_1 + \Theta_{ME}$. Substituting equations (2) and (3) into this expression and solving for Δt_1 yields

$$\Delta t_1 = \frac{\Theta_{ME}(t_d)}{\Omega_S - \Omega_E}. \quad (4)$$

Similar arguments can be made starting with the geometry in Figure 1b to derive the following expression for Δt_2

$$\Delta t_2 = \frac{2\pi - \Theta_{ME}(t_d)}{\Omega_S - \Omega_E}. \quad (5)$$

The weights are given by

$$w_{1,2} = \frac{\Delta t_{2,1}}{27.27}. \quad (6)$$

Note that interpolated measurements with larger time differences have smaller weights.

Prior to the arrival of MAVEN EUVM at Mars, the above described interpolation method was needed to estimate solar irradiance incident on the Mars atmosphere from observations made at Earth. Solar active region emission intensity evolves nonlinearly [Aschwanden, 2006], hence, linear interpolation of their emitted irradiance is prone to error. Further, the effects of variability over very short timescales such as those of flares can only be studied if the emitting region (e.g., flaring site) is visible from both planets. The newly available EUV irradiance measurements at Mars made by EUVM provide new opportunities to study the effects of short-term EUV irradiance variability and are independent of the error associated with linear interpolation.

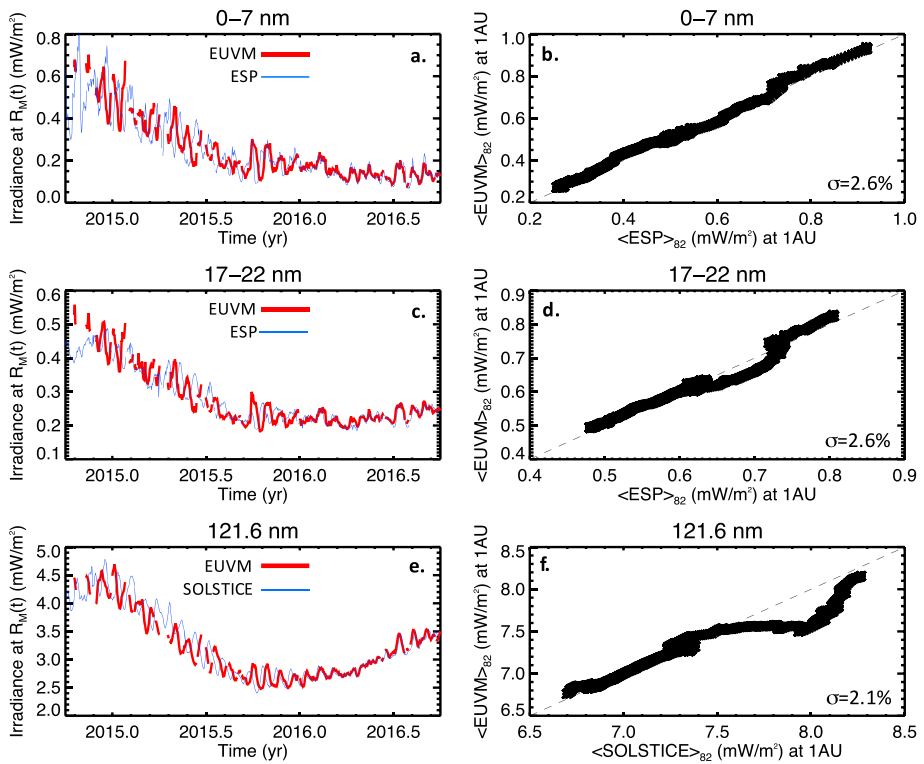


Figure 2. (a, c, and e) Measurements made by MAVEN EUVM in thick red and measurements from comparable channels located at Earth in thin blue. The Earth measurements are scaled to $R_M(t)$. (b, d, and f) Scatterplots of 81 day running averages of the comparable EUVM and Earth-based measurements scaled to 1 AU with the 1:1 line shown, and the standard deviations from the 1:1 line are given on each panel in percent.

2.2. Direct Broadband Irradiance Measurements at Mars From MAVEN EUVM

Since long-term spectral irradiance measurements used to cross calibrate any empirical model of solar spectral irradiance variability are only available at Earth, the MAVEN EUVM channels must be cross calibrated against comparable channels in orbit at Earth in order to be used as inputs to FISM-M. Figures 2a, 2c, and 2e compare time series of daily irradiance measurement averages made by the three EUVM channels with those measured by the Earth-based channels against which they are cross calibrated. The EUVM data are shown with thick red lines, whereas the Earth measurements are shown with thin blue lines and have been scaled to $R_M(t)$. The measurement bands are shown above each panel. The 0–7 nm and 17–22 nm EUVM bands are cross calibrated against the 0–7 nm and 17–22 nm bands measured by the EUV SpectroPhotometer (ESP) [Didkovsky et al., 2012], which is part of the SDO EVE instrument suite. The cross calibration is achieved by a simple first-order linear least squares fit of the EUVM in-band counts with the ESP measurements that have been interpolated to Mars using equation (1). Neither of these two bands show signs of optical degradation based on the linear relationship with their Earth-measured (and degradation-corrected) counterparts. The 117–125 nm EUVM band is cross calibrated with 121.6 nm H I Lyman alpha measurements made by the SOLar Stellar Irradiance Comparison Experiment (SOLSTICE) on board the SOLar Radiation and Climate Experiment (SORCE) [McClintock et al., 2000]. This EUVM band shows some degradation with an exponential decay time constant of 2252 days. The cross calibration of the 117–125 nm EUVM band is done by first interpolating SOLSTICE measurements to Mars using equation (1). Next, average ratios of the SOLSTICE irradiance to EUVM counts for the first 60 day EUVM measurements are available and used to find the initial instrument response. The degradation function decay constant is found using average ratios of the SOLSTICE irradiance to EUVM counts over the 60 days near Earth–Mars opposition (22 May 2016) to determine the decay constant. Note that approximately 90% of the signal measured by the 117–125 nm EUVM band lies in the 121–122 nm range and the cross calibration with SOLSTICE Lyman alpha measurements implies that reported irradiances are for the 121.6 nm Lyman alpha emission line. As such, this band is also referred to as the Lyman alpha or 121.6 nm band.

The time series in Figures 2a, 2c, and 2e capture the three dominant components of spectral EUV variability at Mars. The short-term oscillations are due to solar rotation and have a calculated synodic Carrington period at Mars of approximately 26.35 days, which is shorter than the calculated 27.28 day period for Earth because of Mars's longer orbital period. The steep decrease in irradiance from late 2014 through late 2015 is due to a combination of the declining solar cycle and increasing $R_M(t)$. Mars reached aphelion on 20 November 2015. As such, the irradiance decreased to a lesser degree as $R_M(t)$ began to decrease. Beginning in 2016, an irradiance increase can be seen in the 17–22 nm and 121.6 nm bands indicating that the variability due to $R_M(t)$ is dominating (matching) the solar cycle decline for the 121.6 nm (17–22 nm) band during this period. On the other hand, the 0–7 nm band continues to decrease indicating that the solar cycle decline is slightly larger than the $R_M(t)$ variability for this band.

Figures 2b, 2d, and 2f show scatterplots of the EUVM measurements and the Earth-based measurements against which the EUVM bands are calibrated. Note that all data are scaled to 1 AU. To remove error induced from solar rotations, Earth measurements are angularly interpolated to Mars using equation (1). Because equation (1) does not account for variability occurring at hourly and daily timescales due to solar active region emergence and flares, both EUVM and Earth data are smoothed with an 81 day (approximately three solar rotations) moving average to find the long-term cross-calibration uncertainty. The 1:1 line is shown with a dotted line, and the standard deviation from this line is reported on each panel in percent and are 2.6% for both the 0–7 nm and 17–22 nm bands and 2.1% for the 121.6 nm band. We take these standard deviations to be the long-term cross-calibration uncertainty. Note that the measurement noise, as measured in flight at 1 s cadence, is less than 0.02% and considered negligible [Thiemann, 2016a].

This cross calibration allows FISM-M to be implemented using the EUVM bands. The methodology is described in section 4 in detail but is briefly sketched here. Regression coefficients are found between spectral irradiance measurements (e.g., SDO EVE) and the three aforementioned ESP and SOLSTICE measurements. The regression coefficients are then used to find the irradiance at Mars with the EUVM bands. Next, we describe the data used to develop and drive FISM-M followed by a description of the FISM-M model.

3. Data Sources

3.1. MAVEN EUVM

FISM-M uses measurements from MAVEN EUVM, when available, to estimate spectral irradiance at Mars. MAVEN EUVM measures solar irradiance in three bands selected to characterize EUV emissions from distinctly different regions of the solar atmosphere. The 0.1–7 nm band measures irradiance from hot coronal sources, and solar flares in particular; the 17–22 nm band measures irradiance from the nonflaring corona; and the band centered on 121.6 nm measures the bright H I Lyman α line which is formed in the chromosphere and transition region and forms at temperatures ranging from approximately 6000 K to 25,000 K [Aschwanden, 2006]. The 0–7 nm and 17–22 nm EUVM bands are sensitive to plasmas that form at approximately 6.3–16 MK and 0.3–2.0 MK (FWHM), respectively, as determined by convolving the channel response functions with synthetic isothermal solar plasma spectra from the CHIANTI atomic database [Landi *et al.*, 2011].

The EUVM measurement cadence is 1 s, and EUVM measures solar irradiance continuously except when MAVEN is in eclipse or when both MAVEN is below 500 km and the Sun is in the direction of spacecraft motion. The approximate solar measurement duty cycle is 60% or 2.7 (typically continuous) hours out of every 4.5 h orbit. EUVM also has reduced observations during deep dip campaigns when the spacecraft lowers periapsis 15–30 km below its nominal 150 km periapsis to make in situ measurements near the homopause. These occurred approximately every 3 months for the first 2 years that MAVEN was at Mars. Periods of extended data outages are evident by the gaps in EUVM time series shown in Figure 2.

This paper uses and discusses the Version 8, Revision 1 MAVEN EUVM Level 2 and FISM-M data products. These data sets are publicly archived and distributed by the NASA Planetary Data System, Planetary Plasma Interactions Node (<http://ppi.pds.nasa.gov>).

3.2. Spectral Irradiance Data

The spectral irradiance data sets used to find the proxy regression coefficients, or calibrate, FISM-M from 0.1–6 nm and above 106 nm use data from SORCE, SEE, and the Upper Atmosphere Research Satellite (UARS) and are discussed in Chamberlin *et al.* [2007, 2008]. From 6 to 106 nm, FISM-M is calibrated against SDO EVE Version 5 data at 0.1 nm resolution made by the MEGS A and B channels, and this spectral range is the focus

Table 1. Earth/EUVM Cross-Calibrated Channels Used to Drive FISM-M^a

Primary OP Proxy	CAL and Secondary OP Proxy	SORCE and SEE Era CAL Proxy	Tertiary OP Proxy
L2 0.1–7 nm	SDO/ESP v5 0.1–7 nm	SEE/XPS v11 Ti	L2 17–22 nm
L2 17–22 nm	SDO/ESP v5 17–22 nm	None	L2 121.6 nm
L2 121.6 nm	LASP Lyman α composite ^b	LASP Lyman α composite ^b	Mg II c/w
Mg II c/w ^c		N/A	$F_{10.7}$

^aThe Earth channel serves as a secondary operational proxy when the EUVM data are unavailable. The Tertiary OP proxy is used if the Primary OP and Secondary OP proxies are unavailable.

^bScaled by 1.04 to agree with SORCE SOLSTICE. See text for details. LASP, Laboratory for Atmospheric and Space Physics.

^cOnly used when Primary L2 and Secondary OP proxies are unavailable.

of this paper. The MEGS A channel has (absolute) uncertainties ranging from 10 to 20%. The MEGS B channel has (absolute) uncertainties near 6% for the bright emission lines, the intermediate intensity lines have uncertainties between 10 and 20%, and the low-signal interline regions have uncertainties from 40 to 100%. Above 93 nm, the interline uncertainties exceed 100% because of very low signals and instrument degradation. The FISM-M Daily Model uses Level 3 data from the start of the EVE mission on 3 April 2010 until the failure of the 6–37 nm channel (MEGS A) on 27 May 2014; this failure also corrupted the Version 5 calibration of 35–105 nm channel (MEGS B). The FISM-M Flare Model uses flares with a Geostationary Operational Environmental Satellite (GOES) X-Ray Sensor (XRS) classification of M Class or greater [Bornmann et al., 1996] appearing in the SDO EVE Level 2 Version 5 data, resulting in 431 flares in the 6–37 nm range and 66 flares in the 37–106 nm range. The reduced number of flares on the longer wavelength channel is due to a reduced duty cycle of MEGS B discussed in section 1.

3.3. Proxy Data

As previously stated, FISM-M is calibrated using measurements available at Earth and implemented using the EUVM channels to predict irradiance at Mars; this results in a need for two distinct types of proxies which we distinguish by the names Calibration (CAL) and Operation (OP) proxies. The Level 2 data from the EUVM Channels are the nominal OP proxies. If EUVM data are unavailable, OP proxies are interpolated from Earth using equation (1). The proxies against which the EUVM channels are calibrated are continuing to be measured and, if available, are used as redundant OP proxies. Otherwise, the Bremen Composite Mg II core-to-wing ratio (c/w) [Snow et al., 2014] and $F_{10.7}$ radio flux (reported by the Dominion Radio Astrophysical Observatory in Penticton, British Columbia) are used.

Table 1 shows this hierarchy and the proxies and data versions used. The second and third columns show the CAL proxies used to find regression coefficients with the EVE, SORCE, and SEE spectral irradiance data sets. Table 1 also captures the following redundancy sequence: If the Primary OP Level 2 proxy are unavailable, the Secondary OP proxy in the same row is used. If the Secondary OP proxy is also not available, then the Tertiary OP proxy in the same row is used. If the Tertiary OP proxy is also unavailable, the sequence repeats with the Tertiary OP proxy in place of the Primary OP proxy in column 1. For example, if the Tertiary OP proxy is Level 2 17–22 nm and it is also unavailable, the SDO ESP v5 17–22 nm data are used if available. Ultimately, Mg II c/w is used, and if it is unavailable, $F_{10.7}$. Note that flags in the publicly released EUVM spectral irradiance data indicate whether EUVM or Earth measurements are used as model inputs.

4. FISM-M Model Description

FISM-M is designed to use the MAVEN EUVM channels as proxies to drive the model directly from measurements at Mars. Aside from the input proxies, the primary difference between FISM-M and FISMv1 is in the 6–106 nm range, where different spectral irradiance data sets are used to calibrate the model. FISMv1 models spectral irradiance from 0.1–190 nm at 1 nm resolution and has been calibrated using TIMED SEE from 0.1 to 117 nm and UARS SOLSTICE above 117 nm. FISM-M is similar to FISMv1 outside of 6–106 nm but the FISMv1 legacy regression coefficients are scaled to match the calibration of the EUVM channels which adds additional uncertainty. In the 6–106 nm range, FISM-M has improved 0.1 nm resolution and is calibrated by SDO EVE. In the current version, the 0.1 nm model output is rebinned to 1 nm for release in the EUVM FISM-M data product, but future releases and studies may include the 0.1 nm resolution version. Therefore, 0.1 nm model results and uncertainties are also presented in this section.

FISM-M decomposes the spectral irradiance at 1 AU for the i th wavelength bin, $E(\lambda_i, t)$, over four timescales according to equation (7).

$$E(\lambda_i, t) = E_{\min,i} + \Delta E_{sc,i} + \Delta E_{sr,i} + \Delta E_{ip,i} + \Delta E_{gp,i}, \quad (7)$$

where $E_{\min,i}$, $\Delta E_{sc,i}$, and $\Delta E_{sr,i}$ are the solar minimum, solar cycle, and solar rotation terms that together constitute the daily irradiance model and are described in section 4.1. $\Delta E_{ip,i}$ and $\Delta E_{gp,i}$ are the impulsive and gradual-phase flare terms that together constitute the flare irradiance contribution to the total irradiance and are described in section 4.2. FISM-M also decomposes the input proxies into the same components and finds regression coefficients between the spectral irradiance and proxies for each term on the right-hand side of equation (7) at 1 AU. Since equation (7) estimates irradiance at 1 AU, it must be scaled by $1/R_M^2(t)$ to estimate the irradiance at Mars. As previously stated, all reported EUVM data products are scaled to the Mars-Sun distance.

It is important to note that although FISM-M results are produced at 1 min cadence, the 1 min data are calibrated for flare irradiance and currently do not accurately model nonflaring subdaily variability.

In the remainder of this section, the FISM-M daily and flare model descriptions are presented separately because investigations tend to focus on an atmosphere's response to variability at one of these timescales but typically not both. Each subsection (section 4.1 for the daily model and section 4.2 for the flare model) is organized identically with algorithms, model calibration, model uncertainty, and special measures for adapting FISMv1 legacy regression coefficients in sections 4.1.1 and 4.2.1, 4.1.2 and 4.2.2, 4.1.3 and 4.2.3, and 4.1.4 and 4.2.4, respectively.

4.1. FISM-M Daily Model Description

4.1.1. Daily Model Algorithms

The FISM-M daily irradiance for the i th wavelength bin is given by the first three terms on the right-hand side of equation (7), where the solar cycle and rotation terms are written explicitly as

$$\Delta E_{sc,i} = \langle E_{d,i} \rangle_{108} - E_{\min,i} \quad (8)$$

and

$$\Delta E_{sr,i} = E_{d,i} - \langle E_{d,i} \rangle_{108}, \quad (9)$$

where $E_{d,i}$ is the daily minimum irradiance and $\langle E_{d,i} \rangle_{108}$ is its 108 day average. The terms are modeled by the following set of first-order linear equations relating them to the j th solar cycle and rotation proxies, $P_{sc,j}$ and $P_{sr,j}$, respectively:

$$\Delta E_{sc,i} = E_{\min,i} (b_{sc,ij} + m_{sc,ij} P_{sc,j}) \quad (10)$$

and

$$\Delta E_{sr,i} = E_{\min,i} (b_{sr,ij} + m_{sr,ij} P_{sr,j}), \quad (11)$$

where, using the same notation as in equations (8) and (9),

$$P_{sc,j} = \frac{\langle P_j \rangle_{108} - P_{\min,j}}{P_{\min,j}} \quad (12)$$

and

$$P_{sr,j} = \frac{P_{d,j} - \langle P_j \rangle_{108}}{P_{\min,j}}. \quad (13)$$

$b_{sc,ij}$ and $m_{sc,ij}$ are the (offset and slope) regression coefficients for modeling the solar cycle component (with the i th wavelength bin with the j th proxy), and $b_{sr,ij}$ and $m_{sr,ij}$ are the regression coefficients for modeling the solar rotation component.

4.1.2. Daily Model Calibration

SDO EVE did not observe solar minimum. Instead, $E_{\min,i}$ is found for each 0.1 nm bin by finding the spectral bin minimum daily average values for the entire calibration period and the corresponding MgII c/w values for

those days. Regression coefficients were found from these values which were used to estimate $E_{\min,i}$ from the measured solar minimum value of MgII c/w. Since equations (8) and (9) are overconstrained, $E_{\min,i}$ is not necessarily the best estimate for the minimum irradiance; rather, it is the best estimate of the minimum irradiance from the MgII c/w proxy that is modified with the regression coefficients found using other, possibly better, proxies. For the j th proxy, the model-predicted minimum irradiance is given by $E_{\min,i} \cdot (b_{sc,ij} + b_{sr,ij})$ if we assume that the solar rotation contribution approaches 0 at solar minimum. It should be noted that observations suggest that different wavelengths reach solar cycle minimum irradiance values at different times [Thuillier *et al.*, 2014], an effect that can only be reproduced if a model bin shares the same minimum time with the OP proxy.

The m and b terms in equations (10) and (11) are the model coefficients found by linear least squares fitting of the available CAL proxy and 0.1 nm resolution spectral irradiance data. One hundred nine wavelength bins were too noisy to find meaningful fit coefficients. These excessively noisy bins were identified as bins having $m_{sc,ij} < 0$, indicating that a decreasing measured signal due to uncorrected degradation in the EVE data is masking the expected increasing true signal due to the advancing solar cycle toward solar maximum apparent in the CAL proxy data. Rather than use these known spurious coefficients, $b_{sc,ij}$ is set to 0 and $m_{sc,ij}$ is set equal to $m_{sr,ij}$ for these bins because the long-term degradation is expected to be subtracted from $\Delta E_{sr,i}$ with the removal of the long-term solar cycle variability. We do not quantify the impact of this substitution a priori, but it is likely finite because $m_{sc,ij}$ and $m_{sr,ij}$ are equivalent only if P_j and E_i are formed at similar temperatures in the Sun's atmosphere [Chamberlin *et al.*, 2007]. It is also important to note that setting $b_{sc,ij}$ to 0 can lead to increased model error near solar minimum where this term is expected to become more relevant. However, because these bins correspond with the lowest irradiance in the 6–106 nm range and are multiple orders of magnitude less intense than much of the EUV spectrum, high uncertainties in these bins have minimal impact on the total EUV irradiance as is demonstrated in section 4.1.3. The added uncertainty due to low EVE signal levels and uncorrected degradation is quantified in the EVE data product measurement accuracy, and the added model error resulting from the modified solar cycle regression coefficients is quantified in the FISM-M model uncertainty. Both of these values are incorporated into the FISM-M uncertainty and are discussed in section 4.1.3.

The primary proxy for each 0.1 nm bin is found by evaluating the model at Earth for each proxy for every day that spectral irradiance data are available. The model results are then compared with measurements to select the proxy that minimizes the error for each wavelength bin. The figure of merit used is the standard deviation of the model and measurement fractional difference,

$$\sigma_{ij} = \frac{1}{N} \sqrt{\sum_{d=0}^{N_d} \left(\frac{E_{i,j}(t_d) - E_{i,\text{eve}}(t_d)}{E_{i,\text{eve}}(t_d)} \right)^2}, \quad (14)$$

where $E_{i,j}$ and $E_{i,\text{eve}}$ are the j th proxy-estimated and EVE-measured irradiance for the i th wavelength bin, respectively. The σ_{ij} is also taken to be the uncertainty of the model daily irradiance prediction for the j th proxy.

It is important to note that a smaller σ_{ij} does not necessarily indicate better model performance [Von Storch and Zwiers, 2001]. We use the F test to test whether differences in the model measurement standard deviations are statistically significant and, implicitly, whether the selected primary proxy model with standard deviation, $\sigma_{i,1}$, is expected to perform better than the proxy model with the second smallest standard deviation, $\sigma_{i,2}$. The F test is implemented by computing

$$F = \frac{\sigma_{i,2}^2}{\sigma_{i,1}^2} \quad (15)$$

and comparing it with the critical value, f , for the $F(N_2 - 1, N_1 - 1)$ distribution with 10% significance level, where N_2 and N_1 are the number of samples used to compute $\sigma_{i,2}^2$ and $\sigma_{i,1}^2$, respectively. If $F > f$, the primary proxy is no better than the proxy with the second smallest standard deviation in only 10% of cases. Although FISM-M always uses the proxy with the smallest σ_{ij} , the F test is needed in order to make inferences from the data as is done in the next subsection.

4.1.3. Daily Model Uncertainty

Figure 3 shows the model uncertainty for each 0.1 nm bin driven by each of the three CAL proxy versions of the EUVM bands. The uncertainty is given in percent, absolute units, and 1nm binned percent in Figures 3a–3c, respectively. The triangles at the bottom of Figure 3a correspond with bins where the primary proxy model is

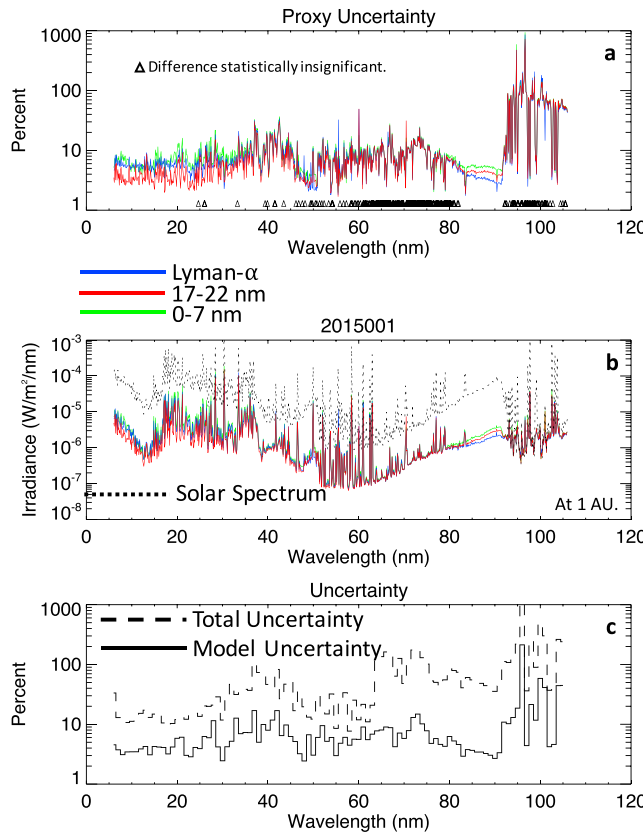


Figure 3. Uncertainties found by comparing FISM-M with SDO EVE measurements. (a) Percent uncertainty for each 0.1 nm bin predicted by the three EUVM proxies. The triangles correspond with bins where the *F* test found that the differences between the smallest and second smallest uncertainties are statistically insignificant. (b) Absolute uncertainty is shown in color, and the FISM-M minimum irradiance spectrum is overplotted with a black dashed line. The values are scaled to 1AU. (c) The 1 nm signal-weighted uncertainty using the minimum model uncertainty for each bin shown in Figures 3a and 3b. The model and total uncertainties are shown with black and dashed lines, respectively.

optimal proxy at the H continuum starting shortward of 92 nm. These H and He emissions form at temperatures more similar to that of the 121.6 nm band, and this band is, therefore, expected to be the statistically optimal proxy for these emissions.

The total uncertainty for the FISM-M daily irradiance, $\sigma_{i,d,\text{total}}$, is the quadrature sum of the uncertainties of the model, the EVE absolute calibration ($\sigma_{i,\text{eve}}$), and the intercalibration of the EUVM channels and the proxies used to calibrate FISM-M ($\sigma_{j,\text{euvm}}$),

$$\sigma_{i,d,\text{total}} = \sqrt{\sigma_{i,\text{model}}^2 + \sigma_{i,\text{eve}}^2 + \sigma_{j,\text{euvm}}^2}. \quad (17)$$

The total uncertainty is shown in Figure 3c. Since $\sigma_{j,\text{euvm}}$ ranges from 2.1 to 2.6% as discussed in section 3.1, $\sigma_{i,\text{eve}}$ dominates the total uncertainty for most wavelengths.

Although $\sigma_{i,\text{model}}$ tends to be less than 10% for much of the 6–106 nm range, there are regions where it exceeds 50%. Figure 3a also shows that the uncertainties undergo a marked increase above approximately 92 nm. This is a result of very low measured signal in these wavelength bins as discussed in section 3.2, and can be seen from Figure 3b which shows the uncertainty and irradiance in absolute units for 1 January 2015; the uncertainties are shown with solid color lines, and the irradiance is shown with a dashed black line. Here we see that the uncertainty drops below 10% for the emission lines but becomes large in the interline region.

not distinguishably better than the proxy model with the second smallest standard deviation as determined by the *F* test. This occurs for 249 bins. For each 0.1 nm bin, the primary proxy is that with the lowest uncertainty shown in Figure 3a. The 1nm binned uncertainty, $\sigma_{j,\text{nm}}$, is the signal-weighted average of the initial 0.1nm binned uncertainties, $\sigma_{i,j}$,

$$\sigma_{j,\text{nm}} = \frac{\sum_{i=j-0.55}^{i=j+0.45} \sigma_{i,j} \cdot E_{i,\text{fism}}}{\sum_{i=j-0.55}^{i=j+0.45} E_{i,\text{fism}}}. \quad (16)$$

Figure 3a shows that the statistically optimal proxies (those with statistically significant smaller standard deviations) are consistent with the expectation that emissions originating from similar regions in the Sun's atmosphere vary similarly [Hinteregger et al., 1981]. Examining wavelengths below 60 nm, where the *F* test identified significant differences in the proxy model variances, we see that the 17–22 nm proxy is the optimal proxy for most bins from 6 to 60 nm. This is consistent with the fact that many of the bins in this region are dominated by emissions from 0.3 MK or hotter plasmas [Phillips et al., 2008] and within the temperature range that the 17–22 nm band is sensitive. However, there are important exceptions where the 121.6 nm band is the statistically optimal proxy, such as the bright He I and II lines at 58.4 nm and 30.4 nm, respectively, and the He I continuum shortward of 50.43 nm. In addition, the 121.6 nm band is also the statistically

Another uncertainty outlier shown in Figure 3c is the bin centered at 63.5 nm. This outlier is from the O V emission line centered at 62.97 nm which lies at the boundary of the 62 and 63 nm bins. FISM-M narrows the broad peak of this line observed by SDO EVE, resulting in less irradiance in the 63.5 nm bin. Because the 63–64 nm range is an otherwise low-signal region, this narrowing of the line by the model results in a relatively significant amount of irradiance being removed from this bin and a net underestimation of the irradiance.

4.1.4. FISMv1 Adaptation to Daily Model

Outside of the 6–106 nm range, the FISMv1 model was driven with Lyman α as the proxy above 106 nm and 0.1–7 nm as the proxy below 6 nm. This requires that the SEE XPS 0.1–7 nm irradiance be recalibrated to match the SDO ESP 0.1–7 nm channel so that the model coefficients can be used by EUVM which is intercalibrated with SDO ESP as discussed in section 3.1. This intercalibration adds an additional 10% uncertainty in quadrature to the 0–6 nm values reported by *Chamberlin et al.* [2007]. Note that no intercalibration is required for using the FISMv1 model coefficients with the EUVM Lyman α proxy because both FISMv1 and EUVM are calibrated against the same (LASP) Lyman α composite.

4.2. FISM-M Flare Model Description

4.2.1. Flare Model Algorithms

The FISMv1 flare model assumes that all subdaily fluctuations are attributed to flaring activity and uses empirical relationships between each 1 nm bin and the GOES XRS 0.1–0.8 nm channel. Similarly, FISM-M uses the 0.1–7 nm EUVM B channel to estimate flare variability at 1 nm resolution based on empirical relationships with 0.1 nm bins. The last two terms on the right-hand side of equation (7) represent the flaring contribution to the total irradiance and are written explicitly as

$$\Delta E_{GP,i} = E_i(t) - E_{d,i} \quad (18)$$

and

$$\Delta E_{IP,i} = \frac{d}{dt} (E_i(t) - E_{d,i}) > 0, \quad (19)$$

where we restrict $\Delta E_{IP,i}$ to having irradiance contributions that are greater than 0. These components are modeled by the 0.1–7 nm proxy, P_{0-7} , and its daily minimum, $P_{d,0-7}$, using

$$\Delta E_{GP,i}(t) = C_{GP,i} (P_{0-7}(t) - P_{0-7,d})^{k_{GP,i}} \quad (20)$$

and

$$\Delta E_{IP,i}(t) = C_{IP,i} \left[\frac{d}{dt} (P_{0-7}(t) - P_{d,0-7}) \right]^{k_{IP,i}}. \quad (21)$$

where the C and k power law coefficients are found for the i th wavelength bin and SXR proxy, P_{0-7} , by the method of least squares. The derivative in the impulsive phase equations, equations (19) and (21), is an application of the Neupert effect, which is the proportionality between the impulsive flare phase and the derivative of the gradual flare phase [Neupert, 1968] and is similar to what was done with FISMv1.

4.2.2. Flare Model Calibration

FISM-M has been calibrated with 431 flares in the 6–37 nm range and 66 flares in the 37–106 nm range measured by SDO EVE. The reason for the reduction in the longer wavelength range is because MEGS B is operated on a reduced duty cycle to preserve the detector which suffers EUV-induced degradation. The calibration set was restricted to M Class and larger flares, because these flares are known to have a measurable impact on the Mars atmosphere [e.g., *Thiemann et al.*, 2015; *Fallows et al.*, 2015] and including smaller flares increases the overall uncertainty in the model.

Values for $C_{xP,i}$ and $k_{xP,i}$ vary depending on the flare's location on the solar disk for many FISM bins because the emission line-dominated 6–106 nm range is more susceptible to resonance scattering within the solar atmosphere than the bremsstrahlung continuum-dominated 0–7 nm range [*Chamberlin et al.*, 2008]. This results in the tendency of emissions from flares located closer to the limb, which must propagate through a thicker column of solar atmosphere, to have less EUV content than disk center flares for the same SXR irradiance. To account for this limb darkening, the calibration set is subdivided according to disk location, with the *Center*, *Mid*, and *Limbflares* originating from 0° – 29° , 30° – 59° , and 60° – 90° from the disk center, respectively, for the 6–37 nm range. The 37–106 nm range was divided into two subsets with disk center flares originating from 0° – 59° from disk center and limb flares originating greater than 60° from disk center. The smaller sample size

Table 2. Correlation Coefficient Thresholds for Zeroing Out Spurious Model Fits

Range/Phase	Correlation	Sample Size	Likelihood Unrelated	Bins Included
6–36 nm/GP	0.45	129	0.06%	186
37–106 nm/GP	0.3	46	4.2%	460
6–36 nm/IP	0.45	129	0.06%	16
37–106 nm/IP	0.3	46	4.2%	22

for the 37–106 nm range was the reason for using two flare location subsets for these bins instead of three. The number of flares in each category is nearly equal, but there is a bias toward more midflares with 40% in that category and 30% in each of the other two categories.

Model coefficients are found independently for each disk location category. In the current version, the EUVM FISM-M data product through Version 8, Revision 1 did not account for the flare location on the disk because the lack of a solar imaging channel on MAVEN makes estimating the flare location difficult. Therefore, the coefficients corresponding with the midflare calibration set are used for all flare irradiance estimates. This results in a slight underestimation of disk center flare irradiance and a potentially significant overestimation of limb flare irradiance. An algorithm is described in section 6 to estimate flare location from the EUVM measurements and will be incorporated into FISM-M in the future.

Some low-signal bins have a minimal flare response, if any at all, and the model fits for these bins are not meaningful. To prevent introducing additional error into the model, these spurious fits are set to 0 and the assumption of no flare response for these bins is made. Correlation coefficients are found for disk center model fits for each bin, and a threshold is set below which the coefficients are set to 0. The threshold was determined by manually inspecting the model fit scatterplots for each bin to find the minimum value of the correlation coefficient that corresponds with scatterplots that show a discernible flare enhancement. Table 2 shows the correlation coefficient threshold and statistical significance for the MEGS A and B channels for the impulsive and gradual model fits. The rightmost column shows the number of bins included by the correlation threshold. The correlation coefficient threshold differs between the MEGS channels because of the different sample size of observed flares made by the two channels. Note that every bin that has an impulsive component also has a gradual-phase component. From Table 2, we see that many fewer bins have an impulsive phase in addition to the gradual phase.

Figure 4 shows example fits of the peak gradual-phase irradiance for four bins measured by MEGS A. The dominant species and the logarithm of its formation temperature are shown at the top of each panel along with the bin wavelength. The data are split into three populations according to flare location as discussed above, and a unique fit is found for each population. There is less scatter evident in Figure 4 (top row) which corresponds with hotter emissions, and there is less distinction between the center and limb populations for these hotter emissions. The limb-darkening effect is most evident in Figure 4 (bottom right) which corresponds with the coolest, and hence lowest height, emission. Here it is clear that the center flares tend to have more 30.4 nm irradiance than the limb flares for the same 0–7 nm irradiance.

4.2.3. Flare Model Uncertainty

The FISM-M flare model uncertainties are found by first computing the standard deviation of the measurement and fit fractional difference for the impulsive and gradual fits for each 0.1 nm bin power law fit in fractional units, $\sigma_{IP,i}$ and $\sigma_{GP,i}$ respectively.

$$\sigma_{IP,i} = \text{stddev} \left(\left[\vec{\Delta E}_{IP,i,\text{model}} - \vec{\Delta E}_{IP,i,\text{data}} \right] / \vec{\Delta E}_{IP,i,\text{data}} \right), \quad (22)$$

$$\sigma_{GP,i} = \text{stddev} \left(\left[\vec{\Delta E}_{GP,i,\text{model}} - \vec{\Delta E}_{GP,i,\text{data}} \right] / \vec{\Delta E}_{GP,i,\text{data}} \right). \quad (23)$$

The fractional uncertainty for each bin is found by weighting the impulsive and gradual-phase contributions for each bin,

$$\sigma_{\text{flare},i} = \frac{C_{IP,i} \left(\sigma_{IP,i} \left(\frac{d}{dt} (P(t) - P_d(t_d)) \right) \right)^{k_{IP,i}} + C_{GP,i} \left(\sigma_{GP,i} \langle P(t) - P_d(t_d) \rangle \right)^{k_{GP,i}}}{C_{IP,i} \left(\left(\frac{d}{dt} (P(t) - P_d(t_d)) \right) \right)^{k_{IP,i}} + C_{GP,i} \left(\langle P(t) - P_d(t_d) \rangle \right)^{k_{GP,i}}}. \quad (24)$$

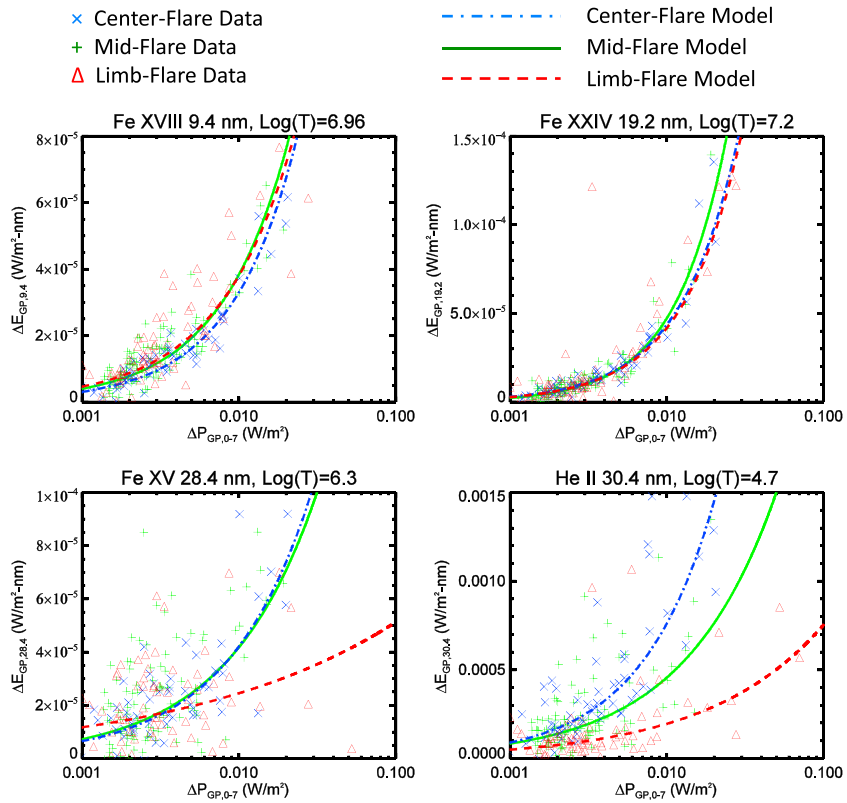


Figure 4. Example bins for the FISM-M gradual-phase fits from MEGS A. The species, wavelength, and log formation temperature are given at the top of each panel. Power law fits are found between the MEGS (vertical axis) and the ESP 0–7 nm (horizontal axis) measured peak gradual-phase irradiance. The symbols and colors correspond with flare location on the disk as discussed in the text, and best fit for each population is shown.

The values for $\sigma_{\text{flare},i}$ are shown in Figure 5a. These values are the 0.1 nm resolution uncertainty in the flare enhancement above the daily value and are binned to the j th 1 nm bin using equation (16). This uncertainty is very large (>100%) in some cases, reflecting the large scatter in the model fits. The total uncertainty for the 1 min cadence FISM-M product is found by adding, in quadrature, the signal-weighted daily and flare contribution uncertainties,

$$\sigma_{1-\text{min}}(t) = \frac{\sqrt{(\sigma_{\text{flare},j} [\Delta E_{\text{IP}}(t) + \Delta E_{\text{GP}}(t)])^2 + (\sigma_j E_d)^2}}{E_d + \Delta E_{\text{IP}}(t) + \Delta E_{\text{GP}}(t)}. \quad (25)$$

An example of the time-dependent FISM-M uncertainty for the 1 min product is shown in Figures 5b and 5c for a magnitude $\times 2$ (at 1AU) flare observed by MAVEN EUVM at Mars. Figure 5b shows the percent uncertainty for the spectrum before the flare and during the flare peak. Figure 5c shows an example of the time-dependent uncertainty for the 13.5 nm and 30.5 nm bins to demonstrate how the uncertainty depends on the proportion of the total irradiance that occurs due to flares.

EUV emissions from lines which form below 10 MK tend to be broader and peak later than SXR emissions [e.g., Woods *et al.*, 2011; Chamberlin *et al.*, 2012]. This is because EUV flare line emissions are from hot plasma that is cooling through a line's formation temperature, and the cooling rate tends to decrease with time [Cargill *et al.*, 1995; Ryan *et al.*, 2013]. Hence, lines with cooler formation temperatures peak later and decay more slowly. Neither FISM-M nor FISMv1 corrects for this effect, and all modeled flare emissions have the same profile as the SXR OP proxy. It is important to note that all reported FISMv1 and FISM-M flare model uncertainties are with respect to the model's ability to estimate the peak flare irradiance. There is additional uncertainty related to the timing of the peak EUV emissions and the total energy deposited that is not currently accounted for in the FISMv1 and FISM-M uncertainty estimates. We cannot give a rigorous characterization of this added uncertainty here, but, qualitatively, EVE data show that the 9.4 nm FeXVIII emission typically peaks hundreds

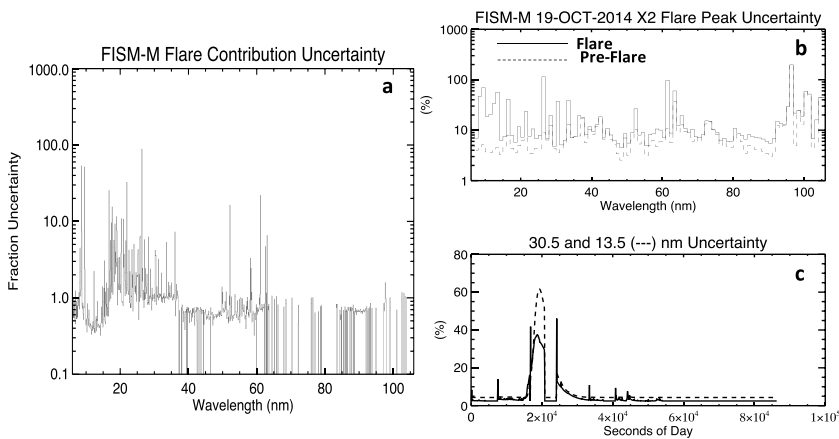


Figure 5. FISM-M flare uncertainty. (a) The fractional uncertainty for the flare model. Note that this is not the subdaily model uncertainty because the flare contribution is a fraction of the total irradiance and the uncertainties must be weighted accordingly. Figures 5b and 5c correspond with an X2 flare observed by EUVM. (b) Spectrum uncertainty for flare and preflare. The uncertainty increases as the proportion of the total irradiance from the flare increases. (c) Example time-dependent uncertainties for the 30.5 nm and 13.5 nm bins.

of seconds after the SXR peak, and FWHM values are approximately 2 times larger for the relatively hot 9.4 nm FeXVIII light curve than the SXR light curve. These effects are exacerbated for cooler emission lines.

4.2.4. FISMv1 Adaptation to Flare Model

For bins outside of the 6–106 nm range, the FISM-M flare component model adjusts the model coefficients of FISMv1 using a cross calibration of the FISMv1 GOES XRS 0.1–0.8 nm proxy and the FISM-M EUVM 0.1–7 nm proxy. This cross calibration was implemented by first finding a zero-offset power law relation between the XRS and ESP derived proxies for flare irradiances exceeding 10^{-5} W/m² (M Class) using the method of least squares. The XRS and ESP cross calibration have associated uncertainties of 55% and 37% for the gradual and impulsive phases, respectively. The conversion from the ESP proxy (either gradual or impulsive), p_e , to the XRS proxy, p_x , is of the form

$$p_{x,j} = m_j \cdot p_{e,j}^{b_j}, \quad (26)$$

where $m_j = 0.0324$, $b_j = 1.14$, $m_G = 0.0154$, and $b_G = 1.23$, and the subscript j corresponds with the impulsive and gradual phases designated by J and G , respectively. The flare irradiance contribution to the i th wavelength bin is of the form

$$\Delta E_i = c_x p_x^{\alpha_x}, \quad (27)$$

where the subscript x indicates that the values are calibrated for an XRS-derived proxy. Equation (26) can be substituted into (27) to find the model coefficients to be used with p_e where we use the subscript e to indicate coefficients that are calibrated for an ESP proxy. Specifically,

$$c_e = c_x \cdot m^{\alpha_x}, \quad (28)$$

$$\alpha_e = b \cdot \alpha_x, \quad (29)$$

where the flare contribution to the irradiance in the i th wavelength bin is now given by

$$E_i = c_e p_e^{\alpha_e}. \quad (30)$$

The coefficients for the FISM-M flare model in the wavelength range outside of the 6–106 nm range are found by applying equations (28) and (29) to the FISMv1 flare model coefficients. The XRS and ESP cross-calibration uncertainty found above is raised to the power α_e to give the added uncertainties to the model irradiance from cross calibration for the gradual and impulsive phases, $\sigma_{G,\text{cross-cal}}$ and $\sigma_{I,\text{cross-cal}}$, respectively. For bins above 106 nm, $\sigma_{G,\text{cross-cal}}$ and $\sigma_{I,\text{cross-cal}}$ are approximately 62% and 47%, and below 6 nm they are approximately 48% and 32%, respectively.

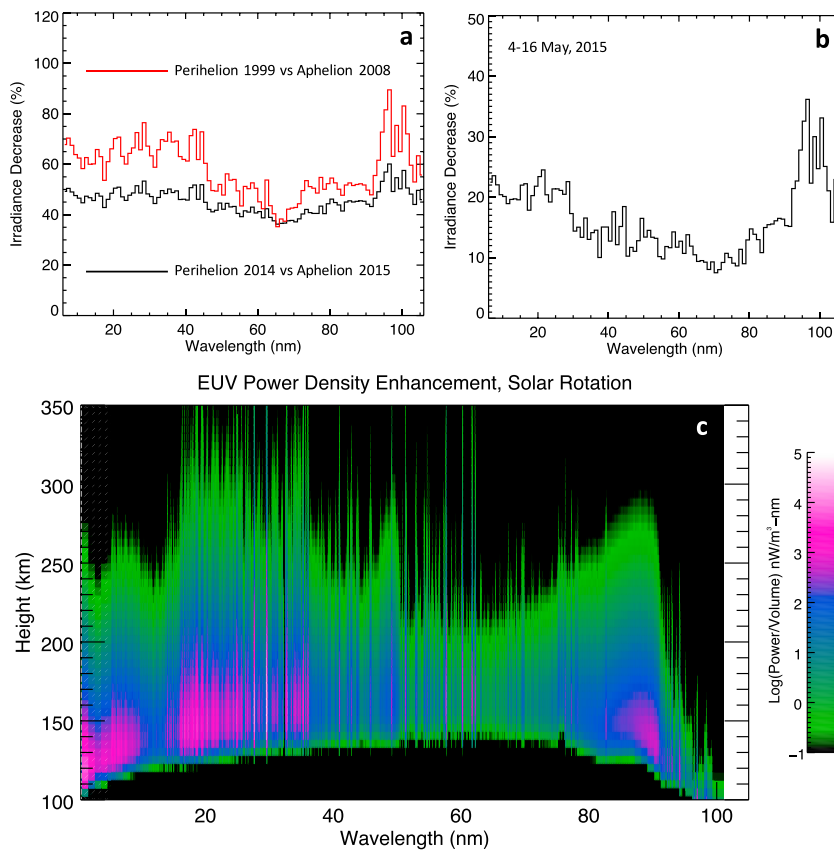


Figure 6. Example results for the FISM-M daily model. (a) The percent decrease from maximum at perihelion to minimum at aphelion during the MAVEN mission in black and solar cycle 23 in red for comparison. (b) The percent decrease from maximum to minimum during a single solar rotation observed in May 2015. (c) The ionization enhancement in the Mars atmosphere due to solar rotation.

5. FISM-M Results

5.1. Sample Daily Model Results

Sample FISM-M daily model results are shown in Figure 6. Figures 6a and 6b show the percent decrease in spectral irradiance at Mars from maximum to minimum values, $(\max - \min)/\max \times 100\%$, over solar cycle and solar rotation timescales, respectively. Figure 6a shows the decrease from perihelion to aphelion observed during the nominal MAVEN mission in black. For comparison, the percent decrease from maximum to minimum of the last solar cycle (23) are shown in red, again taken at Mars. For SC 23, Mars's orbit eccentricity resulted in SC maximum irradiance occurring near perihelion on 12 October 2001 and minimum irradiance occurring near aphelion on 25 June 2008. Comparing the two curves shows that despite the current weak solar cycle, MAVEN was making observations during a period that saw changes in daily average EUV irradiance comparable to what occurred during Solar Cycle 23. However, the spectral decrease is flatter for the period during the MAVEN mission than the preceding solar cycle. This is because much of the difference observed during the MAVEN mission is driven by the changing Mars-Sun distance, which accounts for approximately 40% of the decrease, rather than by solar activity. On the other hand, the spectral dependence of solar activity-driven variability causes the structure seen in the Solar Cycle 23 curve. Figure 6b shows the irradiance decrease due to a single solar rotation occurring in May 2015. In this case, the variability is almost entirely due to a short-term decrease in solar activity because the Mars-Sun distance did not change significantly. This activity dependence causes a more structured spectral decrease, with wavelengths below 30 nm undergoing a 20% decrease over 12 days, while wavelengths near 70 nm change by less than 10%.

Figure 6c shows the enhancement in absorbed power per unit volume or, simply, the *power density enhancement* from the solar rotation as a function of altitude and wavelength at 0.1 nm resolution. To create this figure, a Chapman production function, P_c [Schunk and Nagy, 2009], is computed for each 0.1 nm bin, and the brighter

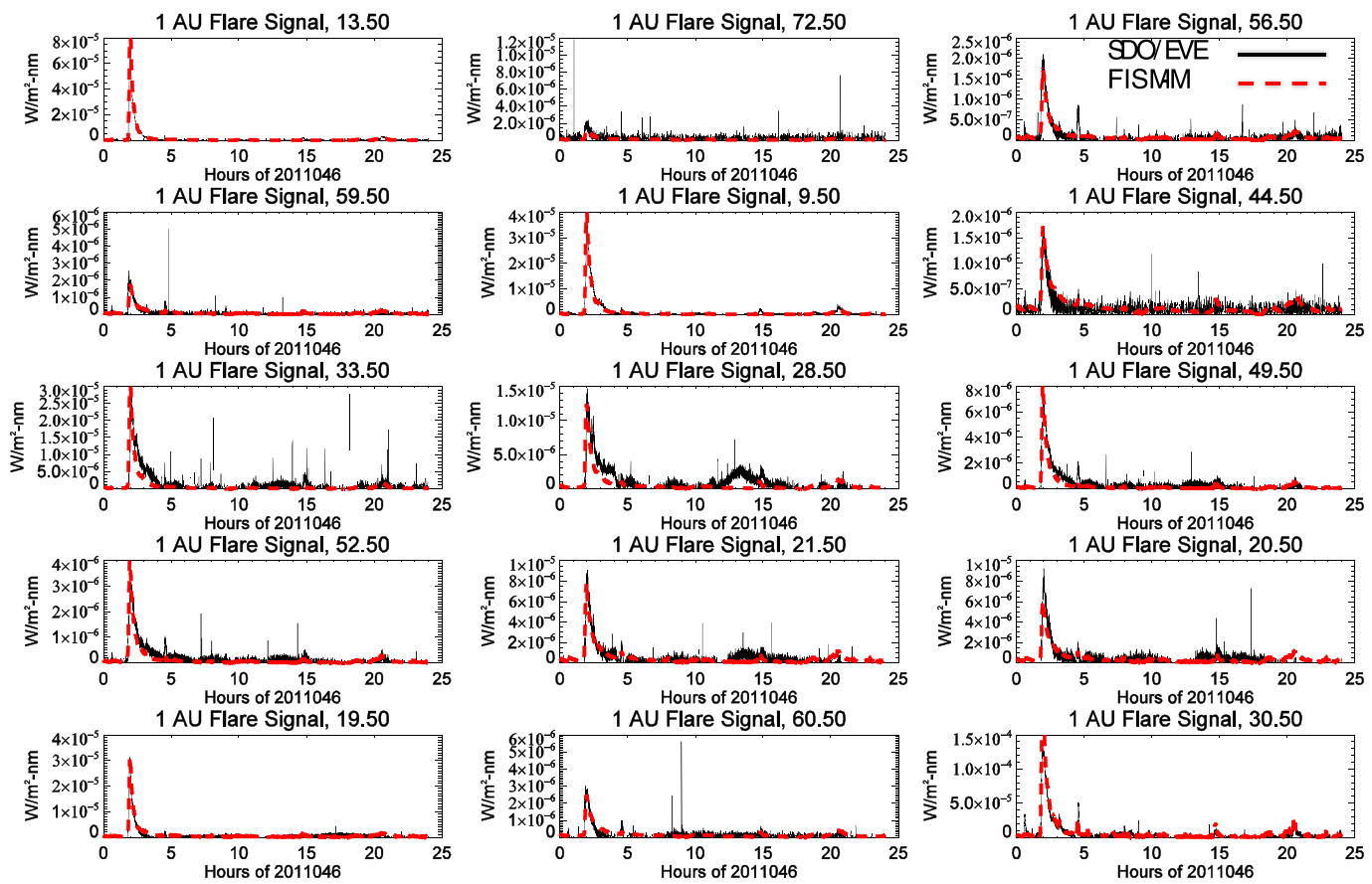


Figure 7. FISM-M run at Earth compared against SDO/EVE for year-day 2011046.

colors correspond with regions of higher ionization per volume of atmosphere (This figure was inspired by an analogous figure for Earth's upper atmosphere in *Solomon and Qian [2005]*). Specifically, for a given wavelength and altitude bin, P_c is the product of the local solar intensity (in units of power per surface area), neutral gas species densities and their respective ionization cross sections, and quantifies the power absorbed at that wavelength and altitude. This power density is found for the solar rotation maximum and minimum, and the difference is the power density enhancement. The Mars neutral atmosphere, limited to only CO₂, O, CO, N₂, and O₂, is simulated by the Mars Global Ionosphere-Thermosphere Model (MGITM) [Bougher et al., 2015b] for $L_s = 0$ and $F_{10.7} = 130$ at 27.5° and 2.5° longitude and latitude with respect to the subsolar point. This position is near the MAVEN periapsis for early May 2015, and the orbital and solar conditions are similar to the actual May 2015 conditions when Mars was near $L_s = 335$ and $F_{10.7}$ ranged from 101 to 166. The spectral regions that correspond with the largest power density enhancement are below 40 nm, which is densely populated with coronal lines, and the 85–90 nm H continuum region. The EUV enhancement from 17 to 25 nm and the He II 30.4 nm emission line has a peak deposition near 150 km, whereas the EUV enhancement shortward of 10 nm and between 85 and 90 nm is deposited lower in the atmosphere, near 130 km due to the ionization cross sections decreasing with wavelength.

5.2. Flare Model Sample Results

Figure 7 shows example results for fifteen 1 nm bins from FISM-M run at Earth (and driven with the CAL proxies) in red compared with SDO EVE data in black for 15 February 2011 which includes an X2.2 flare near 02:00 UT. The bin wavelength in nm is shown above each panel. FISM-M and SDO EVE are in relatively good agreement for the X2.2 flare during the rising phase and flare peak, but FISM-M underpredicts the duration of the decay phase for some lines (e.g., 28.5 nm and 33.5 nm) as discussed in section 4.2.3. The 28.5 nm bin shows a substantial increase in irradiance near 12:00 UT not captured by FISM-M. This demonstrates the limitations of FISM-M for modeling nonflaring subdaily irradiance. The feature does not appear in the FISM-M output because it did not appear in the 0.1–7 nm data, likely because it was due to an event that heated plasma to the formation

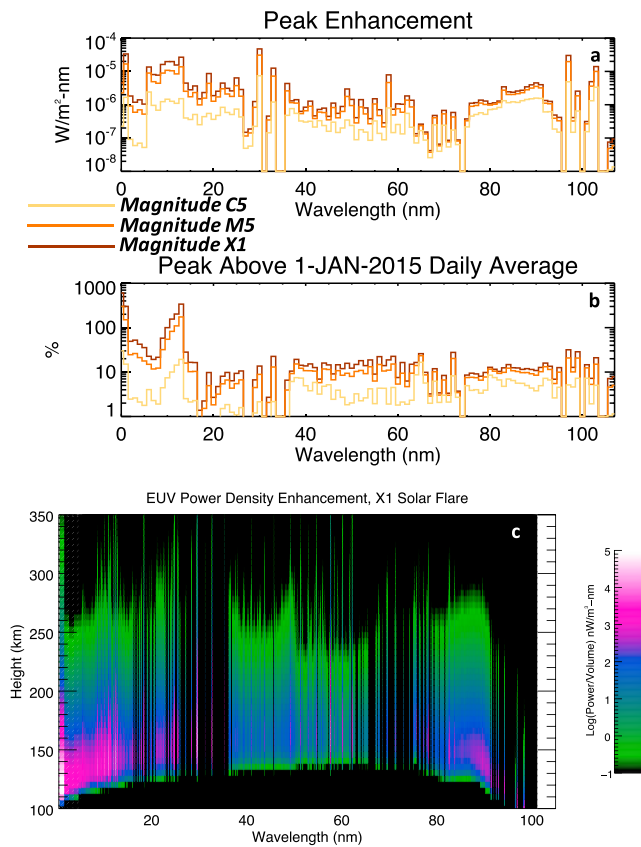


Figure 8. Example FISM-M flare results for magnitude C5, M5, and X1 flares from 0.1 to 106 nm. (a) The peak flare irradiance at Mars on 1 January 2015 and (b) the enhancement over the daily average. (c) Where in the Mars atmosphere the irradiance enhancement from an X1 flare is deposited.

due to the SXRs, and these wavelengths show a significant enhancement. The He II 30.4 nm enhancement is deposited somewhat higher with a peak near 150 km, and the 9–15 nm enhancement peaks near 135 km. Above 97.3 nm, the EUV emissions penetrate deeper into the atmosphere because the more tenuous O₂ is the only major species with finite ionization cross sections at these longer wavelengths.

6. FISM-M Future Improvements

Future versions of the EUVM FISM-M data product should have improvements that correct for some of the known deficiencies stated above. We briefly discuss four high priority improvements that will be implemented in the coming year.

As discussed in section 4.2, limb flares tend to have a reduced EUV spectral content when compared to disk center flares for the same SXR irradiance, and distinct sets of model coefficients are found to correspond to different flare locations. FISMv1 accounts for flare location by using information derived from Earth-based solar X-ray imagers unavailable to FISM-M when a flare is not visible from Earth. Therefore, FISM-M must estimate the flare location without imaging observations to locate a flare. We propose an algorithm for coarse flare location based on the relative intensities of the optically thin EUVM Level 2 0.1–7 nm and optically thick Lyman α measurements. Figure 9 shows scatterplots of Earth-measured 0.1–7 nm and 121.6 nm peak flare irradiances made by SDO ESP and the GOES EUV Sensor E (EUVS-E) channel [Viereck et al., 2007]. They have been sorted into two populations, those originating inside and those originating outside of 45° of disk center. Power law fits that predict the Lyman α irradiance for a given 0.1–7 nm irradiance are found for each population and are overplotted. These curves, with equations shown in the legend, partition the scatterplot into three

temperature of Fe XII, which dominates the 28.5 nm bin, but not to temperatures that result in significant SXR emissions.

Figure 8 shows FISM-M results for three test flares with magnitudes C5, M5, and X1 at Mars. Note that the magnitude ratings are with respect to 1 AU. The spectral irradiance is shown in Figure 8a and modeled for Mars on 1 January 2015. Figure 8b shows the percent of the daily average for the peak of each flare on the same day. The increase of 6–106 nm integrated irradiance is 2.5%, 9.4%, and 14.7% larger than the 1 January 2015 daily average for the C5, M5, and X1 flares, respectively. From Figure 8a, we see that the 30.5 nm bin, which includes the bright He II 30.4 nm line, has the highest peak flare contribution, followed by the 1.5 nm SXR bin. From Figure 8b, we see that the 0.5 nm SXR bin shows the largest percent increase. This increase is rivaled by the 9.5–13.5 spectral region which contains many emissions from highly ionized Fe. This same region and its neighboring bins show a distinct enhancement feature in Figure 8a. Figure 8c shows the X1 flare power density enhancement as a function of wavelength and altitude using the same reference atmosphere discussed in section 5.1. Here we see that the most intense increase occurs near 120 km

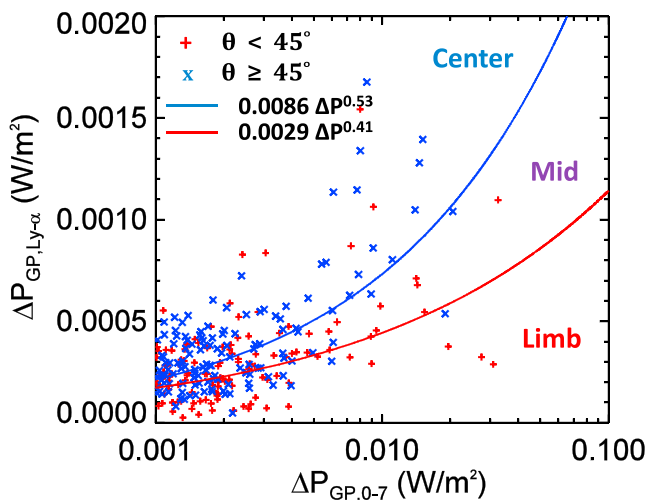


Figure 9. Data and curves used to determine flare location based on the relative response of the EUVM Lyman α and 0.1–7 nm channels. Fits are found of the training set flares with a 0.1–7 nm signal above 1 mW/m² for those within 45° from center and those outside of 45° from center. These curves are taken to the boundaries between Center, Mid, and Limb flares. Source data to determine this relation are from the ESP 0.1–7 nm and GOES-15 EUVS-E Lyman α channels.

at a higher time cadence as a minutely nonflaring component. However, the SXR contribution to the EUVM 17–22 nm channel can be suitably removed at the timescales of an orbit average. This will then be interpolated to a higher time cadence and used to estimate a nonflaring component in future versions of the EUVM FISM-M data product.

A third improvement will reduce uncertainty in impulsive and transition region flare emissions by using the Lyman α channel in addition to the nominal 0.1–7 nm channel for the FISM-M flare component. The intense He II 30.4 nm flare emission is a particular example where using Lyman α as a flare proxy will likely reduce the flare model uncertainty because the two emissions originate from similar regions in the Sun's atmosphere. An added benefit of using this emission as a proxy for emissions that show flare limb darkening is that using the flare location to correct for this effect may become unnecessary because the Lyman α flare proxy limb darkens. This should inherently account for the limb-darkening effect in modeled emissions derived from it.

A fourth improvement will correct for the broadening and peak delay seen in EUV emission lines when compared to SXR emissions. Thiemann [2016b] showed that a single-pole low-pass filter with the appropriate time constant will modulate SXR solar flare light curves to match those of EUV emissions. This technique will be applied to future versions of the MAVEN EUVM FISM-M data product.

7. Summary and Conclusions

FISM-M reproduces daily average irradiance calibrated against SDO EVE observations in the 6–106 nm range by using the EUVM measurements as proxies for solar spectral irradiance variability. The model uncertainty in this range for daily averaged irradiance is less than 5% for most wavelength bins, and the larger total uncertainty is largely driven by the uncertainty in the data sets used to calibrate the model. Uncertainties during flares depend on the size of the flare and increase as the flare contribution becomes larger; sample X2 flare irradiances are below approximately 50% for most 1 nm model bins. FISM-M predicts the average peak EUV flare irradiance measured by SDO/EVE for a given SXR irradiance. We find that the 6–106 nm irradiance increases by 2.5%, 9.4%, and 14.7% for C5, M5, and X1 flares, respectively.

We presented examples of EUV variability observed during the MAVEN primary mission. We showed that the maximum change in irradiance below 50 nm observed during the primary MAVEN mission is approximately 50% smaller than variations over the past two solar cycles due in part to the relative weakness of the observed solar maximum and the fact that the observations during Mars aphelion occurred during relative

regions that are designated “Center,” “Mid,” and “Limb.” Relative peak flare intensities measured by EUVM will be programmatically compared with these curves to estimate the flare location, and the appropriate set of location-dependent FISM-M flare coefficients will be applied.

A second improvement involves modeling nonflaring subdaily variability. FISM-M currently predicts daily average irradiance and flaring EUV irradiance but does not predict nonflaring subdaily variability. This is because the EUVM 17–22 nm channel also has a SXR component that must be removed, and this is done through filtering over daily timescales because it is ambiguous whether sample-to-sample variability is from a change in the 17–22 nm band or the SXR contribution. Therefore, the FISM-M daily (nonflaring) model cannot simply be implemented

moderate solar conditions. We expect that the maximum observed change will increase when MAVEN makes measurements at Mars during the coming aphelion when solar activity is expected to be nearer minimum levels. We also showed that the enhanced EUV power density in the Mars atmosphere is comparable during the strong solar rotation of May 2015 and a hypothetical X1 flare. Early MAVEN results reported changes to the Mars atmosphere in the past due to both of these phenomena [e.g., *Forbes et al.*, 2006 and *Thiemann et al.*, 2015], and FISM-M spectra can be used to better characterize these changes.

The availability of high time cadence EUV spectra for the MAVEN mission should improve the quality of science enabled by the MAVEN mission by capturing the full structure and variability of EUV irradiance, reducing the uncertainty associated with using Earth-derived spectra and activity indices as was necessary prior to the arrival of MAVEN at Mars.

Acknowledgments

This work has been funded by the NASA MAVEN mission, contract NNN10CC04C. E.M.B.T. thanks S. Xu for providing the ionization cross sections used for calculating atmospheric power density spectra. E.M.B.T. also thanks the anonymous reviewers for their thorough feedback which resulted in an improved paper. All EUVM data sets used in this paper are available through the NASA Planetary Data System (PDS). All datacubes containing the MGITM model neutral densities used in this paper are available on the public version of the MAVEN Science Data Center (SDC) website at LASP (<https://lasp.colorado.edu/maven/sdc/public/pages/models.html>). FISM-M model coefficients were submitted as supporting information for this article and are archived by AGU Journals for use by other scientists. Portions of the work used the CHIANTI Atomic Database; CHIANTI is a collaborative project involving George Mason University, the University of Michigan (USA), and the University of Cambridge (UK).

References

- Aschwanden, M. (2006), *Physics of the Solar Corona: An Introduction With Problems and Solutions*, New York, Berlin.
- Bornmann, P. L., D. Speich, J. Hirman, L. Matheson, R. Grubb, H. A. Garcia, and R. Viereck (1996), GOES X-ray sensor and its use in predicting solar-terrestrial disturbances, in *Proceedings SPIE's 1996 International Symposium on Optical Science, Engineering, and Instrumentation*, International Society for Optics and Photonics, pp. 291–298, SPIE-The International Society for Optical Engineering, Denver, Colo.
- Bougher, S. W., et al. (2016), The structure and variability of Mars dayside thermosphere from MAVEN NGIMS and IUVS measurements: Seasonal and solar activity trends in scale heights and temperatures, *J. Geophys. Res. Space Physics*, 122, 1296–1313, doi:10.1002/2016JA023454.
- Bougher, S., T. Cravens, J. Grebowsky, and J. Luhmann (2015a), The aeronomy of Mars: Characterization by MAVEN of the upper atmosphere reservoir that regulates volatile escape, *Space Sci. Rev.*, 195(1–4), 423–456.
- Bougher, S., D. Pawlowski, J. Bell, S. Nelli, T. McDunn, J. Murphy, M. Chizek, and A. Ridley (2015b), Mars Global Ionosphere-Thermosphere Model: Solar cycle, seasonal, and diurnal variations of the Mars upper atmosphere, *J. Geophys. Res. Planets*, 120, 311–342, doi:10.1002/2014JE004715.
- Cargill, P. J., J. T. Mariska, and S. K. Antiochos (1995), Cooling of solar flares plasmas. 1: Theoretical considerations, *Astrophys. J.*, 439, 1034–1043.
- Carr, M. H., and J. W. Head (2003), Oceans on Mars: An assessment of the observational evidence and possible fate, *J. Geophys. Res.*, 108, 5042, doi:10.1029/2002JE001963.
- Carrington, R. C. (1858), On the distribution of the solar spots in latitudes since the beginning of the year 1854, with a map, *Mon. Not. R. Astron. Soc.*, 19, 1–3.
- Chaffin, M. S., et al. (2015), Three-dimensional structure in the Mars H corona revealed by IUVS on MAVEN, *Geophys. Res. Lett.*, 42(21), 9001–9008, doi:10.1002/2015GL065287.
- Chamberlin, P., R. Milligan, and T. Woods (2012), Thermal evolution and radiative output of solar flares observed by the EUV Variability Experiment (EVE), *Sol. Phys.*, 279(1), 23–42.
- Chamberlin, P. C., T. N. Woods, and F. G. Eparvier (2007), Flare irradiance spectral model (FISM): Daily component algorithms and results, *Space Weather*, 5(7), S07005.
- Chamberlin, P. C., T. N. Woods, and F. G. Eparvier (2008), Flare irradiance spectral model (FISM): Flare component algorithms and results, *Space Weather*, 6(5), 1–6.
- Chassefière, E., and F. Leblanc (2004), Mars atmospheric escape and evolution: interaction with the solar wind, *Planet. Space Sci.*, 52(11), 1039–1058.
- Chaufray, J.-Y., et al. (2015), Study of the Martian cold oxygen corona from the O I 130.4 nm by IUVS/MAVEN, *Geophys. Res. Lett.*, 42(21), 9031–9039, doi:10.1002/2015GL065341.
- Deighan, J., et al. (2015), MAVEN IUVS observation of the hot oxygen corona at Mars, *Geophys. Res. Lett.*, 42(21), 9009–9014, doi:10.1002/2015GL065487.
- Didkovsky, L., D. Judge, S. Wieman, T. Woods, and A. Jones (2012), EUV spectrophotometer (ESP) in Extreme ultraviolet Variability Experiment (EVE): Algorithms and calibrations, *Sol. Phys.*, 275(1), 179–205.
- Eparvier, F., P. Chamberlin, T. Woods, and E. Thiemann (2015), The solar extreme ultraviolet monitor for MAVEN, *Space Sci. Rev.*, 195(1–4), 293–301.
- Evans, J. S., et al. (2015), Retrieval of CO₂ and N₂ in the Martian thermosphere using dayglow observations by IUVS on MAVEN, *Geophys. Res. Lett.*, 42(21), 9040–9049, doi:10.1002/2015GL065489.
- Fallows, K., P. Withers, and G. Gonzalez (2015), Response of the Mars ionosphere to solar flares: Analysis of MGS radio occultation data, *J. Geophys. Res. Space Physics*, 120(11), 9805–9825, doi:10.1002/2015JA021108.
- Forbes, J., S. Bruinsma, F. Lemoine, B. Bowman, and A. Konopliv (2006), *Variability of the satellite drag environments of Earth, Mars and Venus due to rotation of the Sun*, Abstract SA22A-04 presented at 2006 Fall Meeting, vol. 1, 4 pp., AGU, Keystone, Colo.
- Haider, S., and K. Mahajan (2014), Lower and upper ionosphere of Mars, *Space Sci. Rev.*, 182(1–4), 19–84.
- Hinteregger, H. E., K. Fukui, and B. R. Gilson (1981), Observational, reference and model data on solar EUV, from measurements on AE-E, *Geophys. Res. Lett.*, 8(11), 1147–1150.
- Hock, R., P. Chamberlin, T. Woods, D. Crotser, F. Eparvier, D. Woodraska, and E. Woods (2012), Extreme ultraviolet Variability Experiment (EVE) Multiple EUV Grating Spectrographs (MEGS): Radiometric calibrations and results, *Sol. Phys.*, 275(1–2), 145–178.
- Jain, S. K., et al. (2015), The structure and variability of Mars upper atmosphere as seen in MAVEN/IUVS dayglow observations, *Geophys. Res. Lett.*, 42(21), 9023–9030, doi:10.1002/2015GL065419.
- Jakosky, B. M., and R. J. Phillips (2001), Mars' volatile and climate history, *Nature*, 412(6843), 237–244.
- Jakosky, B. M., et al. (2015), The Mars Atmosphere and Volatile Evolution (MAVEN) mission, *Space Sci. Rev.*, 195(1–4), 3–48.
- Landi, E., G. Del Zanna, P. Young, K. Dere, and H. Mason (2011), CHIANTI-An atomic database for emission lines. XII. Version 7 of the database, *Astrophys. J.*, 744(2), 99.
- Lean, J. (1997), The Sun's variable radiation and its relevance for Earth 1, *Ann. Rev. Astron. Astrophys.*, 35(1), 33–67.

- McClintock, W. E., G. J. Rottman, and T. N. Woods (2000), Solar Stellar Irradiance Comparison Experiment II (SOLSTICE II) for the NASA Earth Observing System's Solar Radiation and Climate Experiment Mission, in *International Symposium on Optical Science and Technology*, pp. 225–234, International Society for Optics and Photonics, San Diego, Calif.
- Neupert, W. M. (1968), Comparison of solar X-ray line emission with microwave emission during flares, *Astrophys. J.*, 153, L59.
- Peterson, W., et al. (2016), Photoelectrons and solar ionizing radiation at Mars: Predictions versus MAVEN observations, *J. Geophys. Res. Space Physics*, 121(9), 8859–8870, doi:10.1002/2016JA022677.
- Phillips, K. J., U. Feldman, and E. Landi (2008), *Ultraviolet and X-Ray Spectroscopy of the Solar Atmosphere*, vol. 44, Cambridge Univ. Press, Cambridge.
- Rahmati, A., D. Larson, T. Cravens, R. Lillis, P. Dunn, J. Halekas, J. Connerney, F. Eparvier, E. Thiemann, and B. Jakosky (2015), MAVEN insights into oxygen pickup ions at Mars, *Geophys. Res. Lett.*, 42(21), 8870–8876.
- Richards, P., J. Fennelly, and D. Torr (1994), EUVAC: A solar EUV flux model for aeronomic calculations, *J. Geophys. Res.*, 99(A5), 8981–8992.
- Richards, P. G., T. N. Woods, and W. K. Peterson (2006), HEUVAC: A new high resolution solar EUV proxy model, *Adv. Space Res.*, 37(2), 315–322.
- Ryan, D. F., P. C. Chamberlin, R. O. Milligan, and P. T. Gallagher (2013), Decay-phase cooling and inferred heating of M-and X-class solar flares, *Astrophys. J.*, 778(1), 68.
- Sakai, S., et al. (2016), Electron energetics in the Martian dayside ionosphere: Model comparisons with MAVEN data, *J. Geophys. Res. Space Physics*, 121(7), 7049–7066.
- Schunk, R., and A. Nagy (2009), *Ionospheres: Physics, Plasma Physics, and Chemistry*, Cambridge Univ. Press, Cambridge, U. K.
- Snow, M., M. Weber, J. Machol, R. Viereck, and E. Richard (2014), Comparison of Magnesium II core-to-wing ratio observations during solar minimum 23/24, *J. Space Weather Space Clim.*, 4, A04.
- Solomon, S. C., and L. Qian (2005), Solar extreme-ultraviolet irradiance for general circulation models, *J. Geophys. Res.*, 110, A10306, doi:10.1029/2005JA011160.
- Thiemann, E. (2016a), Multi-spectral sensor driven solar EUV irradiance models with improved spectro-temporal resolution for space weather applications at Earth and Mars, PhD thesis, Univ. of Colorado, Boulder, Colo.
- Thiemann, E. (2016b), A new relationship between soft X-rays and EUV flare light curves, in *American Astronomical Society*, pp. 302.04, Solar Physics Division Meeting 47.
- Thiemann, E., et al. (2015), Neutral density response to solar flares at Mars, *Geophys. Res. Lett.*, 42(21), 8986–8992, doi:10.1002/2015GL066334.
- Thuillier, G., et al. (2014), The solar irradiance spectrum at solar activity minimum between solar cycles 23 and 24, *Sol. Phys.*, 289(6), 1931–1958.
- Tobiska, W. K., and F. Eparvier (1998), EUV97: Improvements to EUV irradiance modeling in the soft X-rays and FUV, in *Solar Electromagnetic Radiation Study for Solar Cycle 22*, pp. 147–159, Springer, Netherlands.
- Tobiska, W. K., T. Woods, F. Eparvier, R. Viereck, L. Floyd, D. Bouwer, G. Rottman, and O. White (2000), The SOLAR2000 empirical solar irradiance model and forecast tool, *J. Atmos. Sol. Terr. Phys.*, 62(14), 1233–1250.
- Viereck, R., F. Hanser, J. Wise, S. Guha, A. Jones, D. McMullin, S. Plunket, D. Strickland, and S. Evans (2007), Solar extreme ultraviolet irradiance observations from GOES: Design characteristics and initial performance, in *Proceedings of SPIE 6689, Solar Physics and Space Weather Instrumentation II*, pp. 66890K, SPIE, San Diego, Calif., doi:10.1117/12.734886.
- Von Storch, H., and F. W. Zwiers (2001), *Statistical Analysis in Climate Research*, Cambridge Univ. Press, Cambridge, U. K., and New York.
- Woods, T. N., et al. (2000), TIMED solar EUV experiment, *Phys. Chem. Earth Part C*, 25(5), 393–396.
- Woods, T. N., F. G. Eparvier, S. M. Bailey, P. C. Chamberlin, J. Lean, G. J. Rottman, S. C. Solomon, W. K. Tobiska, and D. L. Woodraska (2005), *Solar EUV Experiment (SEE): Mission overview and first results*, vol. 110, A01312.
- Woods, T. N., et al. (2011), New solar extreme-ultraviolet irradiance observations during flares, *Astrophys. J.*, 739(2), 59.
- Woods, T. N., M. Snow, J. Harder, G. Chapman, and A. Cookson (2015), A different view of solar spectral irradiance variations: Modeling total energy over six-month intervals, *Sol. Phys.*, 290(10), 2649–2676.
- Woods, T., et al. (2012), Extreme ultraviolet Variability Experiment (EVE) on the solar dynamics observatory (SDO): Overview of science objectives, instrument design, data products, and model developments, *Sol. Phys.*, 275(1–2), 115–143.